Advanced Materials

ADVANCED MATERIALS
www.advmat.de

RESEARCH ARTICLE

Phase Synergy Enables Low-Power Ferroelectric Switching in HfO_2 Epitaxial Films

Kefan Wang[1] | Liyang Ma[2] | Lijun Wu[3] | Chuanrui Huo[1] | Sijie Zhu[1] | Chuhang Liu[3] | Wen Sun[4] | Weiwei Li[5] | Shi Liu[2] | Yimei Zhu[3] | Shiqing Deng[1,3] | Jun Chen[1]

[1]School of Advanced Materials Innovation, Innovation Center for Materials Genome Engineering, University of Science and Technology Beijing, Beijing, China | [2]Key Laboratory for Quantum Materials of Zhejiang Province, Department of Physics, School of Science, Westlake University, Hangzhou, Zhejiang, China | [3]Condensed Matter Physics and Materials Science Department, Brookhaven National Laboratory, Upton, New York, USA | [4]School of Integrated Circuits, Tsinghua University, Beijing, China | [5]Department of Materials Science and Metallurgy, University of Cambridge, Cambridge, UK

Correspondence: Shi Liu (liushi@westlake.edu.cn) | Yimei Zhu (zhu@bnl.gov) | Shiqing Deng (sqdeng@ustb.edu.cn)

Received: 16 October 2025 | **Revised:** 1 December 2025 | **Accepted:** 18 December 2025

Keywords: Epitaxial films | Ferroelectric switching | Hafnium oxide | Phase synergy

ABSTRACT

HfO_2-based ferroelectric materials have emerged as leading candidates for next-generation non-volatile memory technologies, owing to their nanoscale robust ferroelectricity and complementary metal–oxide–semiconductor (CMOS) compatibility. However, challenges and debates persist in advancing and comprehensively understanding their ferroelectric behavior. In particular, conventional approaches typically regard non-ferroelectric phases as detrimental and primarily focus on suppressing their formation, yet overlooking their potentially synergistic contributions—particularly those of the tetragonal (*T*) phase. Here, we unambiguously clarify the beneficial role of the *T*-phase and introduce a phase-boundary engineering strategy that deliberately harnesses it to enhance ferroelectricity in HfO_2 films. By stabilizing optimal coherent boundaries between ferroelectric orthorhombic (*O*) and *T* phases in epitaxial La-doped HfO_2 films, we achieve significant improvements in ferroelectric properties—doubling the remanent polarization ($P_r \sim 30$ μC/cm^2) and substantially reducing the coercive field ($E_c \sim 3$ MV/cm) by 30% compared to low-La doped samples without such boundaries. Atomic-scale electron microscopy reveals the structural nature of the atomically sharp, coherent *O*–*T* boundaries. Combined with deep-learning enhanced molecular dynamics simulations, our results unravel that these boundaries facilitate intermediate polarization states that lower the switching energy barrier. Consequently, phase coexistence shifts from an inherent drawback to a tunable design element, offering a broadly applicable route to ultra-low-power HfO_2-based nanoelectronics.

1 | Introduction

Ferroelectric memory devices utilize switchable spontaneous polarization for information storage and processing, making them integral to modern electronic technology [1–3]. However, their widespread practical implementation has long been hindered by critical challenges, including poor scalability, high power consumption, and incompatibility with conventional complementary metal-oxide-semiconductor (CMOS) processes [4, 5]. This landscape shifted dramatically with the discovery of ferroelectricity in doped high-κ hafnium dioxide (HfO_2) thin films [6]. Owing to their robust ferroelectricity at nanoscale dimensions and seamless compatibility with CMOS integration, HfO_2-based ferroelectrics have rapidly emerged as

Kefan Wang and Liyang Ma contributed equally to this work.

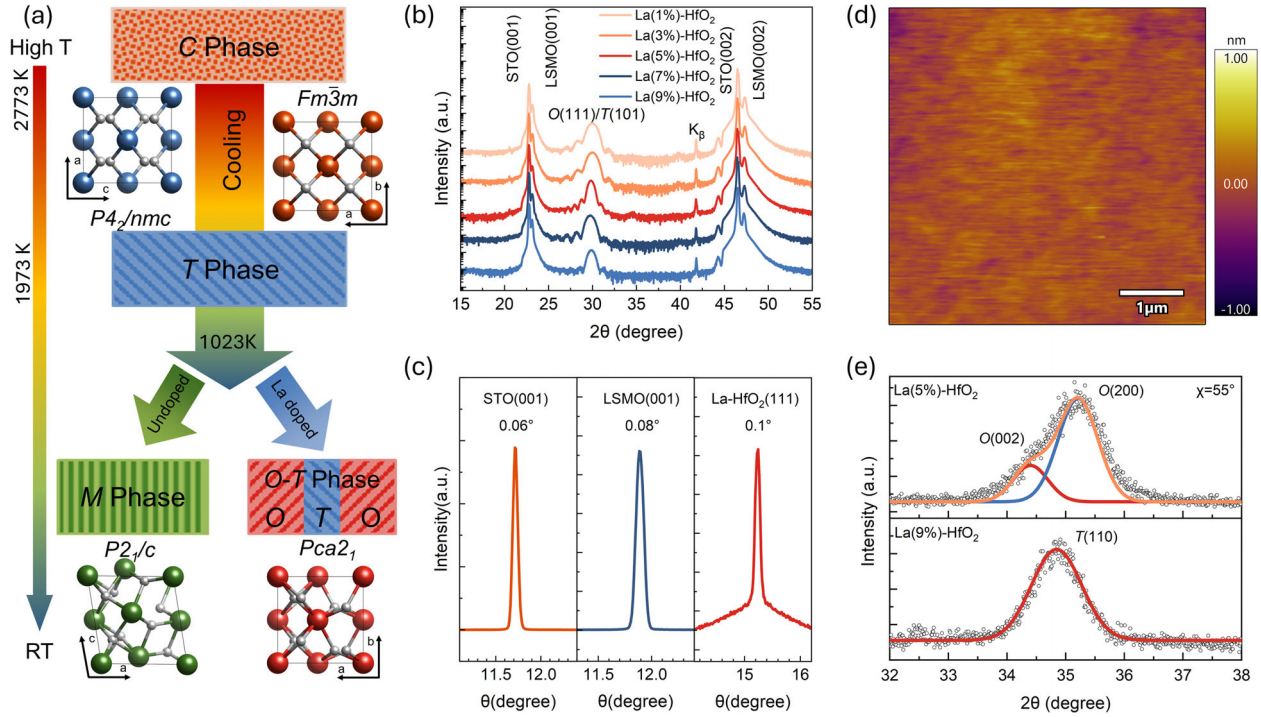

FIGURE 1 | Morphology and structural characterization of La-doped HfO_2 thin films. (a) Schematic diagram for the phase transition in HfO_2-based thin films. (b) XRD θ–2θ patterns of films with varying La doping concentrations. (c) XRD rocking curves of $SrTiO_3$ (STO) substrates, $La_{0.7}Sr_{0.3}MnO_3$ (LSMO) buffer layer, and *O*-La (5%)-HfO_2 (*O*-HLO) thin film. (d) Atomic force microscopy (AFM) image showing the surface morphology of the La (5%)-HfO_2 film. (e) In-plane XRD θ–2θ scans at $\chi = 55°$ for La (5%) and La (9%)-HfO_2 films, highlighting phase differentiation.

leading candidates for next-generation non-volatile memory devices [7–13].

Despite these advantages, unlocking the full potential of HfO_2-based ferroelectrics remains challenging due to their complex polymorphism and the metastable nature of their functional phases. These intrinsic characteristics give rise to critical issues—such as high coercive fields [14], wake-up effects, and fatigue—that continue to impede their practical deployment in memory technologies. HfO_2 exhibits a complex phase diagram that encompasses both thermodynamically stable phases—monoclinic (*M*-phase, $P2_1/c$, room-temperature), tetragonal (*T*-phase, $P4_2/nmc$, above 1973 K), and cubic (*C*-phase, $Fm\bar{3}m$, above 2773 K) [15, 16]—as well as metastable phases, such as orthorhombic (*O*-phase, $Pca2_1$) and rhombohedral (*R*-phase, $R3m$). Among them, the metastable *O*-phase is widely considered to be ferroelectric [15, 17, 18]. Recent studies have also suggested that the high-energy rhombohedral phases, such as $R3m$ and $R3$, may exhibit ferroelectricity under specific conditions [19]. During film growth or thermal processing, HfO_2 typically undergoes a sequence of phase transitions upon cooling from the high-temperature *C*-phase (Figure 1a). The *T*-phase forms first, followed by transformation into either *M*- or *O*-phase at lower temperatures, depending on extrinsic factors such as strain state, chemical doping [20], and film thickness [21]. This dynamic often results in the coexistence of ferroelectric and non-ferroelectric phases—such as *O*–*M* or *O*–*T* phase mixtures— frequently observed in experiments [22, 23]. Consequently, the macroscopic ferroelectric properties are governed not only by the volume fraction of the ferroelectric *O*-phase but also by the competition and interaction between coexisting phases. This complex phase behavior raises two pressing questions: How can the formation of the desired ferroelectric phase be directed over competing non-ferroelectric phases? And can phase interactions be deliberately engineered to enhance ferroelectricity? Addressing these questions is essential for advancing the rational design of high-performance HfO_2-based ferroelectrics.

Traditionally, efforts to enhance ferroelectricity in HfO_2-based systems have focused on maximizing the *O*-phase while suppressing non-ferroelectric phases, particularly the high-temperature *T*-phase, which have been considered detrimental to ferroelectric performance [24]. The presence of such non-ferroelectric phases in HfO_2-based thin films has been associated with undesirable effects like wake-up behavior, fatigue, and endurance degradation [25]. As a result, previous studies have primarily aimed to inhibit the *T*-phase formation and minimize its content during phase transitions by optimizing doping, thermal processing, or film thickness. However, emerging evidence suggests that the *T*-phase can essentially play a more nuanced and dynamic role in regulating ferroelectricity. During crystallization, *T*-phase precursors can kinetically suppress the thermodynamically favored nucleation pathway of the *M*-phase. Through a kinetic confinement effect, the spatially confined *T*-phase serves as a preferential nucleation site for the *O*-phase, thereby promoting its oriented precipitation (Figure 1a) [26]. Additionally, under an applied electric field, the *T*-phase can act as a structural intermediate—either transforming into the *O*-phase that actively modulates the switching pathway or facilitating polarization reversal between the polarization up (*P*+) and polarization down (*P*−) states [27, 28]. Recently, using an in situ grazing incidence X-ray diffraction approach, Chen et al. demonstrated that the *T*-phase

serves as a transient intermediate during polarization switching in the *O*-phase, forming a three-well energy landscape model along the *O*–*T*–*O* pathway. Within this framework, the *T*-phase facilitates polarization reversal by modulating the energy barrier of the reversible *O*–*T* transition, effectively reducing the E_c [29]. Theoretical studies further indicate that this transformation pathway modulates the energy landscape between *P*+ and *P*− states, lowering the energy barrier for switching and contributing to more efficient polarization dynamics [30, 31]. These findings represent a paradigm shift: non-ferroelectric phases such as the *T*-phase, rather than being purely parasitic, can actively enhance ferroelectric performance when properly harnessed. This underscores the critical importance of precise control over the phase composition and architecture to achieve an optimal balance between competing polymorphs. However, this remains challenging due to competing thermodynamic stabilities and kinetic pathways among different phases, necessitating fine-tuned optimization of fabrication processes, such as doping levels [32, 33], annealing protocols, and film geometry [34].

In this study, we demonstrate that precise control over phase composition and interphase architecture can significantly enhance the ferroelectric performance of La-doped HfO_2 epitaxial thin films (La concentration, 1–9 mol%). This is in agreement with previous studies, which show that La-doping in HfO_2 effectively stabilizes the ferroelectric *O*-phase and significantly improves the ferroelectric performance of HfO_2 thin films [35, 36]. In particular, contrary to conventional assumptions that *T*-phase degrades ferroelectricity, our results highlight the beneficial roles of non-ferroelectric *T*-phase in promoting ferroelectric switching and enhancing ferroelectric performance. Specifically, in La (5%)-HfO_2 film, we realized a well-defined *O*–*T* phase coexistence, featuring an optimal interphase architecture of a unique atomically coherent phase boundary. Rather than impeding ferroelectricity, this *O*–*T* phase boundary facilitates ferroelectric switching and significantly improves overall performance. Compared to La (1%)-doped counterparts lacking *O*–*T* phase coexistence, La (5%)-doped HfO_2 films exhibit over a twofold increase in remanent polarization ($P_r \sim 30\ \mu C/cm^2$) and a 30% reduction in coercive field ($E_c \sim 3$ MV/cm). Combining atomic-scale electron microscopy quantification with deep-learning potential molecular dynamics (DPMD) simulations, we uncover the underlying mechanisms: the *O*–*T* phase boundary acts as an energy-relieving pathway during polarization reversal, enabling intermediate polarization states and ultimately lowering the switching energy barrier. Based on these findings, we propose a phase-boundary-assisted switching model and establish a clear link between phase topology, ferroelectricity, and switching dynamics. The insights and approach presented in this study, particularly the recognition and strategic utilization of the critical role of non-ferroelectric phases, offer a new paradigm for designing high-performance HfO_2-based ferroelectric devices.

2 | Results and Discussion

2.1 | Structural Characterizations

Epitaxial La-doped HfO_2 thin films, with La concentrations ranging from 1% to 9%, were deposited on (001)-oriented $SrTiO_3$ (STO) substrates using pulsed laser deposition (PLD). A conductive $La_{0.7}Sr_{0.3}MnO_3$ (LSMO) buffer layer was employed to both facilitate epitaxial growth and serve as the bottom electrode (detailed growth conditions are provided in the Materials and Methods section). The film thicknesses were maintained at ~10 nm, as confirmed by X-ray reflectivity (XRR) (Figure S1) and cross-sectional electron microscopy. Figure 1b presents the X-ray diffraction (XRD) θ–2θ patterns of La-HfO_2 films with varying La doping concentrations. Notably, all films exhibit a distinct diffraction peak near 30°, which is attributed to the (111)−orientated ferroelectric *O*-phase (denoted as $(111)_O$). The presence of well-defined Laue oscillations around the $(111)_O$ diffraction peak indicates the high crystallinity of the films and smooth film-substrate interface. Furthermore, rocking curve (RC) measurements indicate the excellent structural quality of both the La (5%)-HfO_2 thin films and the LSMO buffer layer, with full widths at half maximum (FWHM) below 0.1° (Figure 1c), indicating their high crystallinity. Atomic force microscopy (AFM) measurements further confirm the high quality of the thin films, revealing a root-mean-square surface roughness below 1 nm (Figure 1d) [37].

It is worth mentioning that the diffraction peaks of the orthorhombic $(111)_O$ and tetragonal $(101)_T$ phases—located at approximately 30.15° and 29.66°, respectively—are in close proximity, making it challenging to distinguish them using standard XRD measurements alone [38]. This overlap complicates accurate phase identification in HfO_2-based thin films. To overcome this limitation, one possible approach is the use of χ angle-dependent XRD measurements, where χ refers to the angle between the sample surface normal and the incident X-ray beam. In particular, measurements at $\chi = 55°$ offer improved phase resolution by probing lattice anisotropy in specific crystallographic planes. For the *O*-phase, the lattice parameters along the *a*− and *b*−axes are nearly identical, with a slight difference of approximately 0.2 Å between the *a*/*b* and *c* axes ($a = 5.05$ Å, $b = 5.08$ Å, $c = 5.26$ Å). As a result, when oriented along the out-of-plane [111] direction, two distinct diffraction peaks, corresponding to $(002)_O$ and $(200)_O$, appear with noticeable splitting in the angular range of 34°−35° at an in-plane orientation of $\chi = 55°$ [39], as shown in the upper panel of Figure 1e. In contrast, for *T*-phase—where the lattice parameters satisfy $a = b = 3.65$ Å and exhibit a much larger difference along the *c*-axis ($c = 5.33$ Å)—only a single diffraction peak, corresponding to $(110)_T$, appears in the same angular range when oriented along the [101] direction. This method thus allows for clear differentiation between the diffraction signatures of different phases, enabling effective identification of the phase composition in the HfO_2 samples. For our thin films, the results in Figure 1e show that the La (9%)-HfO_2 film (lower panel) is predominantly composed of the *T*-phase, while the La (5%)-HfO_2 film exhibits a dominant *O*-phase character (upper panel). Note that this method is particularly effective for identifying pure *T*-phase films. However, when the *O*-phase is present, the existence of the *T*-phase may still be ambiguous due to residual peak overlap.

2.2 | Ferroelectric Properties

The electrical performance of La-doped HfO_2 thin films was systematically characterized using the capacitor structure illustrated in Figure 2a. Performance data for films with varied thicknesses and doping levels are provided in Figure S2. The

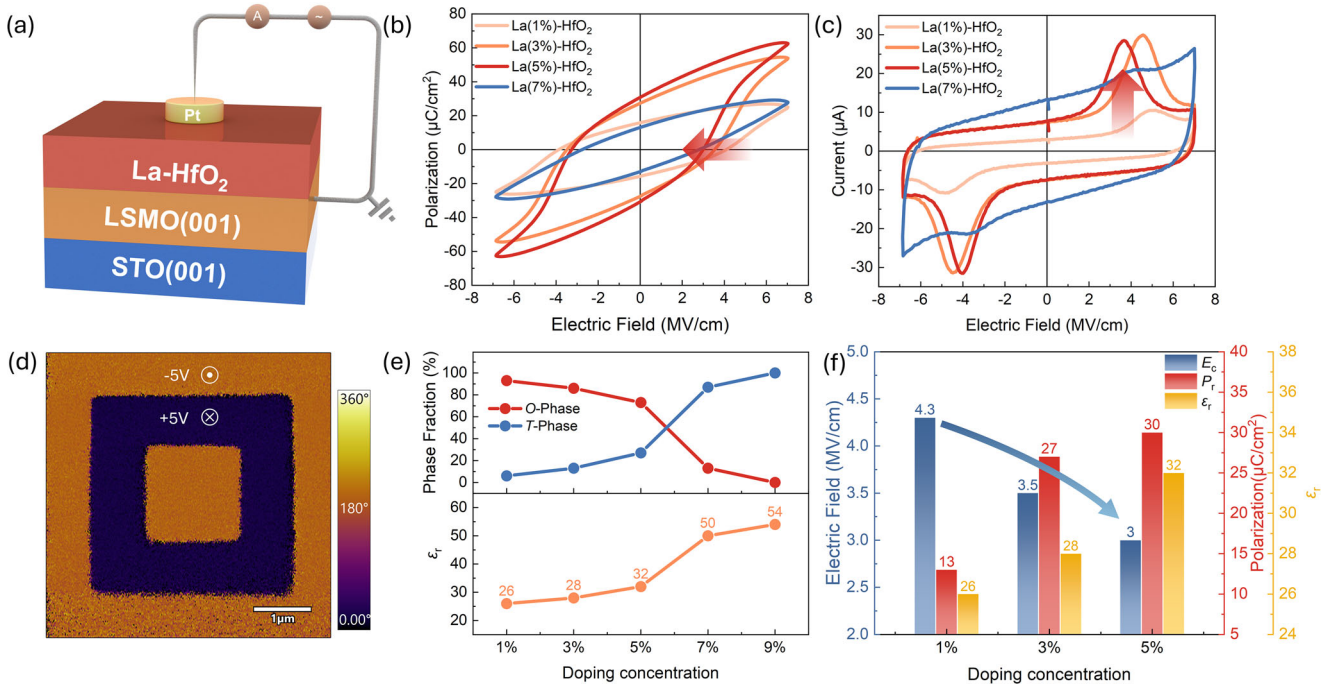

FIGURE 2 | Electrical characterization of La-doped HfO_2 thin films. (a) Schematic diagram of the metal-ferroelectric-metal (MFM) capacitor test structure. (b) Polarization-electric field (*P-E*) hysteresis loops and (c) current-electric field (*I-E*) curves for films with varying La doping concentrations. (d) Piezoresponse force microscopy (PFM) phase image after bipolar polarization with ±5 V. (e) Variation of relative dielectric constant (ε_r) and *O–T* phase ratio as a function of La doping concentration. (f) Summary of coercive field (E_c), remanent polarization (P_r), and ε_r for thin films across different doping levels.

polarization-electric field (*P-E*) hysteresis loops in Figure 2b demonstrate a transition from non-ferroelectric to ferroelectric upon La doping. Even at a doping level as low as 1%, the emergence of ferroelectricity is observed. This transition is primarily attributed to La doping-induced oxygen vacancies, which are recognized to play a crucial role in stabilizing the ferroelectric *O*-phase, consistent with prior reports [40, 41]. Notably, at relatively low doping levels from 1% to 5%, with the increase in La content, the P_r progressively improves, accompanied by increasingly pronounced current switching peaks (Figure 2c). More importantly, the E_c shows a significant reduction, indicating enhanced switching dynamics. However, further increases in doping concentration beyond 5%—specifically at 7% and 9%—lead to a marked deterioration in ferroelectric performance, characterized by reduced hysteresis and elevated leakage currents. This degradation has its origin in the increased prevalence of the non-ferroelectric *T*-phase, as evidenced by the XRD results in Figure 1e. Such variations in ferroelectric performance with La content highlight the La (5%)-HfO_2 film as the optimal composition, yielding the best balance between *O*- and *T*-phase content. This composition exhibits superior ferroelectric properties, with a high $P_r \sim 30\ \mu C/cm^2$ and a low $E_c \sim 3$ MV/cm. The excellent switchability of the La (5%)-HfO_2 film is further confirmed by piezoresponse force microscopy (PFM) measurements (Figure 2d), where bipolar domain patterns are written using an electrically biased tip. Enhanced PFM amplitude signals are observed in the poled regions, and the sharp domain boundaries separate regions of opposite polarization. The up (bright regions) and down (dark regions) polarization states exhibit nearly 180° phase contrast—indicative of stable and reversible ferroelectric switching [42, 43].

Correlating the evolution of ferroelectric properties with structural changes, one can find that the observed performance variations essentially originate from the shifting ratio between *O*- and *T*-phases. This is further substantiated by dielectric spectroscopy measurements in Figure S3, which show a systematic increase in the dielectric constants (measured at 10^4 Hz) with increasing La concentration. Given the substantial differences in dielectric constants between *O*-phase (24–29) and *T*-phase (24–57) [44–46], changes in the relative dielectric constant can serve as a qualitative indicator of the *O*/*T* phase ratio. The increasing dielectric constant suggests a progressive enrichment of the *T*-phase relative to the *O*-phase. Figure 2e, f summarizes the trends in key performance metrics as a function of La doping levels and corresponding phase composition (*O–T* phase ratio). A particularly notable trend is that with the introduction of the *T*-phase and an increase in its proportion, the E_c shows a significant decrease. Specifically, compared to the La (1%)-HfO_2 film, which exhibits predominantly *O*-phase character and negligible *T*-phase, the La (5%)-HfO_2 film—with a higher *T*-phase fraction—shows an ~30% reduction in E_c. This trend suggests that while the *T*-phase itself is non-ferroelectric, its presence plays a functional role in facilitating polarization switching. Specifically, an optimal *T*-phase content appears to lower the energy barrier for domain reversal, enabling more efficient ferroelectric switching while simultaneously enhancing, rather than compromising, the P_r. However, this beneficial effect is confined to a narrow composition window: further increases in the *T*-phase fraction beyond the optimal point (e.g., La >5%) lead to a sharp degradation in ferroelectricity due to the dominance of non-switchable phases. These observations, therefore, raise an important mechanistic question: how does the presence of a non-ferroelectric *T*-phase

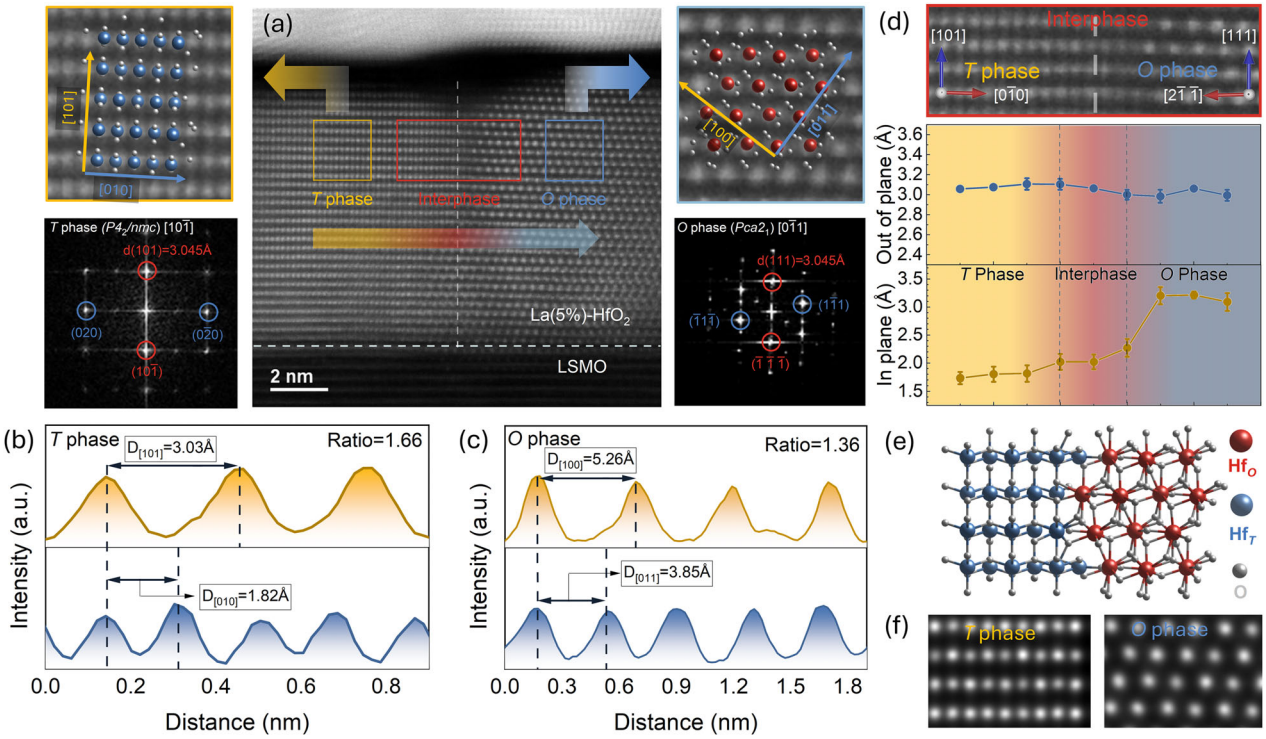

FIGURE 3 | Electron microscopy characterization of La (5%)- HfO_2 films. (a) Cross-sectional HAADF-STEM image of a 10 nm La (5%)-HfO_2 film. FFT patterns from the yellow and blue boxed regions indicate the presence of *T*-phase along the [10$\bar{1}$] zone axis and the *O*-phase along the [0$\bar{1}$1] zone axis, respectively. (b, c) Quantitative lattice spacing ratio analysis for the *T*-phase (b) and *O*-phase (c) along the directions marked in (a). (d) Spatially resolved analysis of the lattice parameters across the domain-matching boundary between *T*- and *O*-phases. (e) Constructed structural model depicting the domain-matching coherent boundary between the $[10\bar{1}]_T$ and $[0\bar{1}1]_O$. (f) Simulated HAADF-STEM image for the $[10\bar{1}]_T$ and $[0\bar{1}1]_O$ phases based on the structural model shown in (e), showing good agreement with experimental data.

reduce the switching barrier in ferroelectric films? To address this, we conducted detailed microstructural investigations of the La (5%)-HfO_2 film, which exhibits the optimal *O*/*T* phase balance.

2.3 | Atomic-scale Characterization

To elucidate the microscopic origin of the reduced coercive field, quantitative atomic-scale analysis was conducted using aberration-corrected scanning transmission electron microscopy (STEM). Figure 3a presents a high-angle annular dark-field (HAADF) image of the La (5%)-HfO_2 film, revealing atomically resolved structural features across a region exhibiting phase coexistence. Fast Fourier transform (FFT) analysis, along with local magnified structural inspection, confirms the coexistence of *T*-phase (left) and *O*-phase (right). Specifically, the *T*-phase is oriented along its [10$\bar{1}$] zone, with an out-of-plane direction of [101], while the *O*-phase is aligned along its [0$\bar{1}$1] zone, with an out-of-plane direction of [111]. Such results are consistent with macroscopic crystallographic characterizations presented in Figure 1, lending further support to the phase assignment. Given the subtle structural differences between HfO_2 polymorphs, unambiguous phase identification requires more than qualitative analysis of HAADF contrast or FFT patterns. To this end, we conducted a detailed measurement of local structural parameters to distinguish the coexisting phases. As shown in Figure 3b, c, the aspect ratio ($D_{(101)}/D_{(010)}$, where $D_{(101)}$ and $D_{(010)}$ denote the corresponding lattice plane spacings) in the *T*-phase region was measured to be ~1.66, closely matching the theoretical value of 1.65 expected for *T*-phase along the [101] zone axis. In contrast, the *O*-phase on the right exhibited an aspect ratio ($D_{(100)}/D_{(011)}$) of ~1.36. Given that the *O*-phase has three possible in-plane orientation variants—[0$\bar{1}$1] (theoretical ratio ~1.37), [10$\bar{1}$] (~1.39), and [1$\bar{1}$0] (~1.47)—the measured value most closely aligns with the [0$\bar{1}$1] orientation [47].

A striking structural feature revealed by the HAADF-STEM image is the formation of a well-defined, atomically coherent boundary between the *O*- and *T*-phases within the La (5%)-HfO_2 film. The two phases establish a coherent domain-matching relationship along the out-of-plane direction. This is further clarified by the quantitative structural analysis at the *O*–*T* phase boundary within the magnified area shown in Figure 3d. Individual atomic columns were fitted using two-dimensional (2-D) Gaussian peaks to accurately extract their positions. From this analysis, we quantified the average out-of-plane (OOP) and in-plane (IP) lattice spacings near the boundary. The OOP lattice spacings in both *T*- and *O*-phases remain continuous and are nearly identical across the phase boundary, confirming that the *O*–*T* phase boundary is coherent without significant strain accumulation. Such coherence promotes effective mechanical and electronic coupling across the phase boundary. Meanwhile, the IP lattice spacings in both phases closely match their respective bulk values, suggesting that the two phases accommodate the underlying substrate effectively through domain matching without generating misfit dislocations. Based on these findings, we constructed

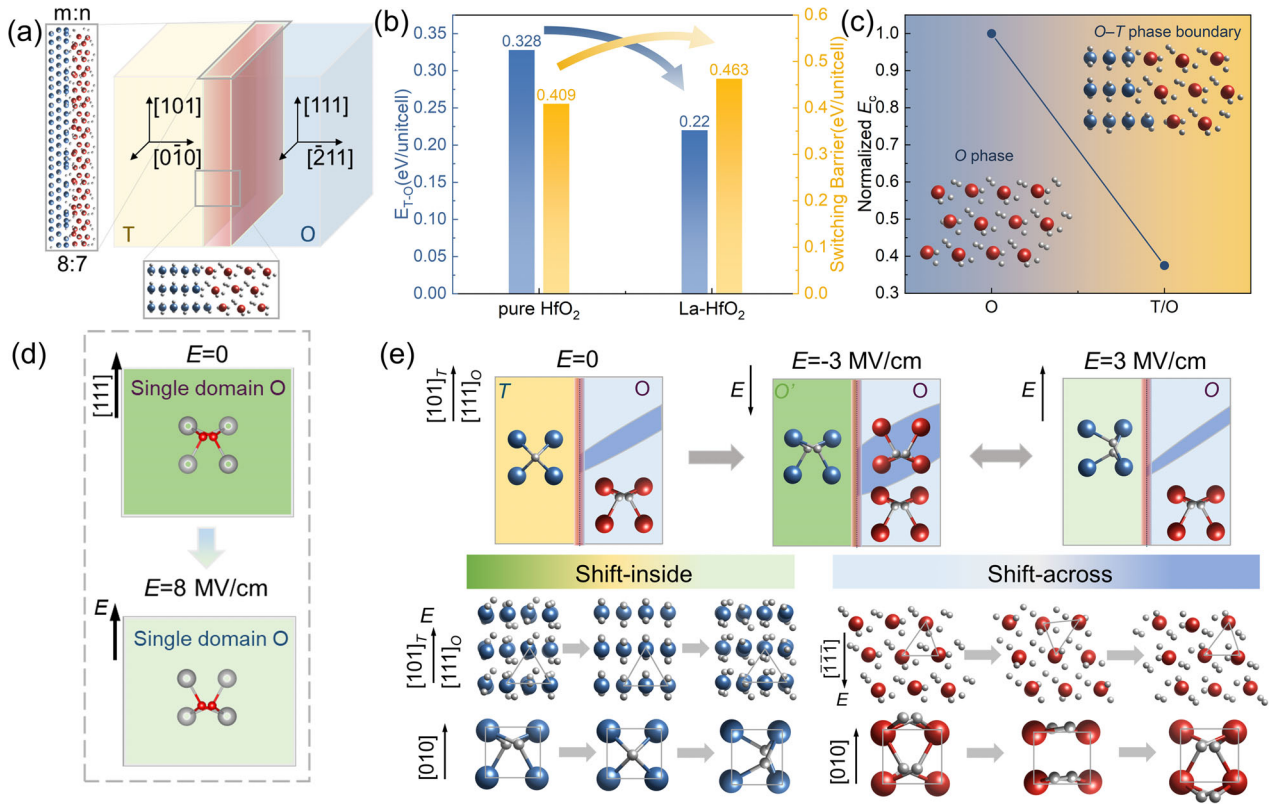

FIGURE 4 | Theoretical insights into the *O*–*T* phase boundary and its role in enhancing polarization switching. (a) Structural model of the *O*–*T* domain-matching structure with a coherent phase boundary. (b) Calculated relative thermodynamic energy and polarization switching energy barrier for the La-doped HfO_2 system. (c) Comparison of coercive field (E_c) between the pure *O*-phase and the *O*–*T* domain-matching structure, highlighting the reduced switching threshold enabled by phase coexistence. (d) A single-domain *O*-phase requires an electric field of ~8 MV/cm to achieve complete polarization switching within 100 ps. (e) Schematic illustration of the proposed phase-boundary-assisted switching (PBAS) model, where polarization switching is mediated through the *O*–*T* phase boundary. A downward electric field of ~3 MV/cm drives *T*-to-*O* transformation (denoted as *O*') via the shift-inside (SI) mechanism, while the partially switched domain within the *O*-phase grain expands through the shift-across (SA) mechanism, forming 180° domain walls that facilitate easier reverse switching of the *O*'-phase through the same SI pathway.

a structural model of the *O*–*T* phase boundary (Figure 3e) and performed HAADF-STEM image simulations using parameters that match the experimental conditions. The simulated images (Figure 3f) accurately reproduce the key features observed in the experimental data, validating the structural model. This coherent *O*–*T* phase boundary model forms the basis for subsequent theoretical investigations presented in Figure 4, where we explore its influence on polarization switching dynamics.

2.4 | Multiscale Theoretical Calculations

To understand how the observed *O*–*T* phase boundary contributes to the performance improvement, we employed a multiscale computational framework that integrates density functional theory (DFT) calculations with deep-learning potential molecular dynamics (DPMD) simulations. DPMD employs a machine-learned potential generated by deep neural networks, which are trained directly on densities, energies, and forces derived from quantum-mechanical calculations. This approach allows DPMD to achieve near first-principles accuracy while maintaining computational efficiency comparable to classical MD, enabling reliable simulations over large spatial and temporal scales. This key advantage is critical for this work, as understanding the kinetic processes underlying phase transition pathways and polarization switching in doped HfO_2 requires both high accuracy and large-scale sampling. The structural model of DPMD simulations is shown in Figure 4a. As a first step, La dopants were incorporated into the *O*-phase lattice (as shown in the configurations in Figures S4 and S5), and the resulting energy changes were computed. The DFT results reveal that La doping effectively reduces the thermodynamic energy difference between the *T*- and *O*- phases—from 0.33 eV/unit cell (in the pristine *O*-phase) to 0.22 eV/unit cell at a doping level of 6.25% La (Figure 4b). This energetic stabilization supports the experimental observation of phase coexistence in the doped system and suggests that La doping promotes *O*–*T* phase boundary formation.

However, a critical discrepancy emerges when examining the polarization switching energy barrier using nudged elastic band (NEB) calculations. Specifically, contrary to experimental results showing a substantial reduction in E_c, the NEB calculations predict a slight increase in the switching energy barrier—from 0.409 eV/unit cell in the undoped *O*-phase to 0.463 eV/unit cell after La doping. This apparent contradiction can be traced to the limitations of the conventional single-phase DFT model, which does not account for the presence of *O*–*T* phase boundaries. These findings suggest that, in the scenario where only the *O*-phase

exists without the *O*–*T* phase boundary, La doping alone into the *O*-phase lattice does not facilitate polarization switching and may, in fact, hinder it. By contrast, the experimentally observed reduction in E_c is likely mediated by the coherent *O*–*T* phase boundary, which introduces an alternative, lower-energy switching pathway. This inconsistency underscores the crucial role of interfacial effects—specifically, domain-matching *O*–*T* phase boundaries—in modulating coercivity and enabling energy-efficient switching. It also highlights the limitations of conventional single-phase DFT models and underscores the necessity for an advanced theoretical framework capable of explicitly incorporating interfacial polarization dynamics and accurately capturing their influence on the macroscopic ferroelectric behavior of doped HfO_2 systems.

We thus turn to DPMD simulations to fully capture how the *O*–*T* phase boundary facilitates the polarization switching. The calculations are based on the structural model derived from experimental observations (Figure 3). The formation of an *O*–*T* phase boundary leads to a 63% decrease in E_c relative to the single *O*-phase (Figure 4c). As illustrated in Figure 4d, in a single-domain *O*-phase, an external electric field of ∼8 MV/cm is required to achieve complete polarization switching within 100 ps. In contrast, the introduction of a domain-matching *O*–*T* boundary dramatically reduces this switching threshold. Specifically, our DPMD simulations reveal that this *O*–*T* phase boundary induces the formation of a partially switched domain (PSD) within the *O*-phase matrix (dark blue region in the right panel in Figure 4e), which serves as a nucleation center for subsequent polarization reversal. Under an applied downward electric field of ∼3 MV/cm, the *T*-phase undergoes a field-induced transformation into the *O*-phase, driven by the motion of oxygen anions opposite to the field direction via the shift-inside (SI) mechanism [17]. To distinguish this transformation product from the intrinsic *O*-phase, we denote it as the *O*'–phase. Simultaneously, the PSD within the *O*-phase expands through the shift-across (SA) mechanism, wherein oxygen anions traverse the hafnium atomic planes—a process previously predicted in several theoretical studies [17, 47]. These results highlight that the presence of the *O*–*T* phase boundary can activate new switching pathways at relatively low electric field strengths. Notably, the PSD in the *O*-phase forms a 180° domain wall with the adjacent *O*'–phase, which facilitates more facile reverse switching. In fact, a reversed electric field of just ∼3 MV/cm is sufficient to switch the polarization of *O*'–phase via the same SI mechanism. Based on these insights, we propose a mechanistic phase-boundary-assisted switching (PBAS) model (Figure 4e), in which the *O*–*T* phase boundary functions not merely as a structural discontinuity, but as an active functional boundary that both initiates and accelerates polarization switching by enabling cooperative SI and SA processes. This PBAS mechanism provides a compelling explanation for the reduced coercive field observed in our experiments and underscores the potential of phase-boundary engineering as a promising strategy for achieving low-power ferroelectric switching in HfO_2-based thin films.

3 | Discussion

Traditionally, the *T*-phase in ferroelectric HfO_2 thin films has been regarded as an undesired byproduct, with most efforts directed toward suppressing its formation to favor the pure *O*-phase state. Our findings overturn this conventional view by clearly demonstrating that the non-ferroelectric *T*-phase can, in fact, play a beneficial—rather than detrimental— role in polarization switching. We show that controlled coexistence of ferroelectric and non-ferroelectric phases at engineered phase boundaries can produce synergistic interactions that enhance switching behavior. In particular, coherent *O*–*T* interfaces boost such interactions by enabling more efficient and strong strain and electronic coupling, thereby facilitating *O*–*T* transformation and markedly promoting polarization reversal. As unambiguously revealed by the combination of atomic-scale characterization and computational simulations, such interfaces not only create a low-energy pathway for polarization switching but also reshape the energy landscape between P^+ and P^- states, thereby accelerating switching kinetics. This mechanistic insight is also independently confirmed from a different perspective using in situ grazing incidence X-ray diffraction, which establishes the *O*–*T*–*O* pathway as the most energetically favorable switching mechanism [27]. These insights redefine the role of non-ferroelectric phases—traditionally viewed as harmful—by establishing them as active contributors to ferroelectric functionality. More broadly, they highlight phase boundaries not as passive structural defects but as dynamic, designable features that regulate polarization switching, offering generalizable design principles for other ferroic systems where competing phases govern functionality.

The selection of La for stabilizing the coherent *O*-*T* boundaries is driven by its unique combination of ionic characteristics, defect chemistry, and epitaxial compatibility. Specifically, La has a relatively large ionic radius (La^{3+}: 1.16 Å), which effectively induces chemical pressure on the HfO_2 lattice, resulting in pronounced local lattice expansion and distortion—key factors in stabilizing the metastable *O* phase. Additionally, the charge mismatch between La^{3+} and Hf^{4+} facilitates the formation of oxygen vacancies, which help stabilize the ferroelectric *O* phase by compensating for charge imbalances and reducing the nucleation barrier. These oxygen vacancies can also perturb the local bonding environment, collectively promoting the formation of *O*–*T* boundary. This interplay between lattice strain and defect chemistry effectively modifies the energy landscape of the *O*–*T* phase transition. As confirmed by our DFT calculations, La doping effectively tunes the energy difference between the *O* and *T* phases, decreasing the energy gap from 0.33 eV per unit cell in undoped HfO_2 to 0.22 eV per unit cell at a 6.25% La concentration (Figure 4b). This modification forms the foundation for fine-tuning the *O*-*T* phase transition and broadens the phase coexistence window. At the optimal doping level, a balance between competing energies—such as surface and interface energy—can favor the coexistence of *O* and *T* phases and promote the formation of coherent *O*–*T* boundaries. Our experimental and theoretical results confirm that the 5% La doping level represents a critical compositional window where thermodynamic phase stability and kinetic switching pathways are optimally balanced. At this doping level, a delicate balance is achieved: sufficient *T*-phase content forms coherent boundaries, which act as active switching pathways through the PBAS mechanism, without compromising the percolating ferroelectric *O*-phase network. However, when La concentration exceeds 5%, the thermodynamic balance shifts too far toward *T*-phase stabilization, leading to the dominance of the non-ferroelectric phase. This disrupts

the continuous *O*-phase network, reducing switchable polarization, introducing additional leakage paths, and ultimately leading to degraded ferroelectric performance at higher doping levels.

Previous studies have consistently shown that the atomic layer deposition (ALD)-grown polycrystalline and multiphase films exhibit significantly lower E_c compared to their PLD-grown counterparts, which tend to be phase-pure [14, 48]. This difference points to the critical role of structures and abundant interfacial regions, which are characteristic of ALD-grown films. In this sense, while this study is based on epitaxial films, the insights extend directly to technologically relevant ALD-grown polycrystalline films. In these industrially important materials, the role of phase coexistence has not been sufficiently considered, partly because the complexity of polycrystalline systems makes it challenging to disentangle the underlying mechanisms. By contrast, epitaxial films provide a clean and well-controlled platform that allows us to unambiguously reveal the beneficial role of phase coexistence, particularly involving the non-ferroelectric phase. These findings establish phase-boundary engineering as a powerful and generalizable strategy for optimizing key ferroelectric parameters, thereby offering new opportunities for the development of low-power, high-performance HfO_2-based memory devices. They also provide a solid conceptual foundation to guide the optimization of polycrystalline hafnia films for practical applications.

4 | Conclusion

This study demonstrates that the coexistence of ferroelectric *O*- and non-ferroelectric *T*-phases—achieved through precise La doping in epitaxial HfO_2 thin films—can significantly reduce the E_c, a critical metric for energy-efficient ferroelectric switching. Specifically, the La (5%)-HfO_2 film, featuring a coherent *O*–*T* phase boundary, exhibits an E_c of 3 MV/cm—approximately 30% lower than that of the predominantly *O*-phase La (1%)- HfO_2 film. Through atomic-resolution electron microscopy and deep-learning molecular dynamics simulations, we reveal that the *T*-phase plays a pivotal role in mediating intermediate polarization states during reversal, thereby effectively optimizing the switching pathway and lowering the energy barrier. These insights challenge the traditional single-phase-centric view of ferroelectricity in HfO_2–based systems and highlight the transformative potential of phase-boundary engineering. Our findings establish a new design principle for tailoring polarization dynamics and lay the groundwork for future development of low-power, high-performance HfO_2–based nanoelectronic and non-volatile memory devices.

5 | Experimental Methods

5.1 | Thin-Film Growth

Epitaxial La-doped HfO_2 thin films were deposited on (001)-oriented $SrTiO_3$ (STO) substrates buffered with a $La_{0.67}Sr_{0.33}MnO_3$ (LSMO) bottom electrode using pulsed laser deposition (PLD) with a KrF excimer laser (λ = 248 nm). The LSMO layer was first grown at 750 °C under an oxygen partial pressure of 18 Pa, using a laser fluence of 1.25 J cm^{-2} and a repetition rate of 3 Hz. Subsequently, La-doped HfO_2 films with doping concentrations ranging from 1% to 9% were deposited at the same substrate temperature under a dynamic oxygen pressure of 13 Pa, using a laser fluence of 1.5 J cm^{-2} and a repetition rate of 2 Hz. After deposition, the heterostructures were cooled to room temperature at a rate of 15°C min^{-1} in 13 Pa oxygen. All ceramic PLD targets were synthesized by a conventional solid-state reaction method. High-purity HfO_2 (99.99%) and La_2O_3 (99.99%) powders were mixed in appropriate ratios, thoroughly ground, and calcined at 1400 °C to ensure complete reaction and target densification powders.

5.2 | Structural Analysis

The structural properties of the La-doped HfO_2 thin films were investigated using high-resolution X-ray diffraction (XRD) with Cu Kα_1 radiation (λ = 1.5406 Å) on a 9 kW Rigaku SmartLab diffractometer. Two distinct scanning geometries were employed to comprehensively characterize the crystallographic structure. First, conventional θ–2θ radial scans were performed to determine the out-of-plane orientation and lattice parameters of the films. This mode provides information on phase identification, crystallographic orientation, and film quality through the observation of diffraction peak positions and Laue fringes. Second, grazing-incidence in-plane diffraction (GIXD) was conducted by tilting the sample along the χ direction and rotating the azimuthal angle φ, while keeping θ–2θ fixed. This configuration enables detailed examination of the in-plane crystallographic symmetry and epitaxial relationships between the film and substrate.

5.3 | Electrical Measurements

Macroscopic electrical properties of the La-doped HfO_2 thin films were evaluated using a metal–ferroelectric–metal (MFM) capacitor configuration. Platinum (Pt) top electrodes were deposited onto the film surface through a shadow mask, while the bottom LSMO electrode, grown on the $SrTiO_3$ substrate, was grounded. All electrical characterizations were conducted using an aixACCT TF3000 ferroelectric analyzer. Specifically, polarization–electric field (*P*–*E*) hysteresis loops and current–electric field (*I*–*E*) characteristics were recorded using a triangular voltage waveform at a measurement frequency of 1 kHz and an applied electric field of 7 MV cm^{-1}, ensuring consistent and reliable evaluation of the ferroelectric switching behavior.

5.4 | DFT Calculations

All density functional theory (DFT) calculations were performed using the Vienna ab initio Simulation Package (VASP) [49] with the projector augmented-wave (PAW) [50, 51] method and the Perdew-Burke-Ernzerhof (PBE) exchange-correlation functional [52]. The optimized lattice constants of *Pca2₁* HfO_2 are a = 5.266 Å, b = 5.048 Å, and c = 5.077 Å, and the polarization is along the c axis (z axis). Structural parameters of unit cells are optimized using a plane-wave cutoff of 600 eV, a 4 × 4 ×

4 Monkhorst-Pack k-point grid for Brillouin zone sampling, an energy convergence threshold of 10^{-6} eV, and a force convergence threshold of 10^{-3} eV/Å. For the 6.25% La-doped system, a 2 × 2 × 2 supercell (containing 30 Hf, 2 La, 63 O atoms, and one oxygen vacancy) was constructed, and a 2 × 2 × 2 Monkhorst-Pack k-point grid was adopted. The thermodynamic energy difference between *T* and *O* phases was evaluated by computing multiple doping configurations and selecting the lowest-energy structure. The minimum energy paths (MEPs) of switching processes are determined using the NEB technique implemented in the Universal Structure Predictor: Evolutionary Xtallography (USPEX) code [53–55], during which the lattice constants are clamped. The stopping criterion for searching the MEP is when the root-mean-square forces on images are less than 0.03 eV/Å.

5.5 | MD Simulations

To investigate the PBAS mechanism, a stoichiometric domain-matched (m/n = 8/7) *O*–*T* model comprising 11700 atoms was constructed, aligned with the experimentally determined lattice orientation for molecular dynamics (MD) simulations. Isobaric-isothermal (NPT) ensemble MD simulations were performed using a deep neural network-based force field [56, 57], with model accuracy benchmarks and sample inputs accessible via an online notebook [17]. All NPT ensemble MD simulations are carried out using Large-scale Atomic/Molecular Massively Parallel Simulator (LAMMPS) [58], with temperature controlled via the Nose ´-Hoover thermostat and the pressure controlled by the Parrinello-Rahman barostat. The equations of motion were integrated with a 1-fs timestep. The electric fields are included in MD simulations using the "force method" [59, 60], where an additional force $\mathcal{F}_i$ is added on the ion i according to $\mathcal{F}_i = Z_i^* \cdot E$, with Z_i^* being the Born effective charge (BEC) tensor of ion i.

Acknowledgements

This work was financially supported by the following funding. The National Key R&D Program of China grant No. 2021YFA1202100 (SL and SD). The electron microscopy work at BNL was supported by the U.S. Department of Energy, Office of Basic Energy Science, Division of Materials Science and Engineering, under Contract No. DE-SC0012704 (YZ, LW, and SD). The National Natural Science Foundation of China grant U24A200 (SD). The National Natural Science Foundation of China grant 22375015 (SD). The National Natural Science Foundation of China grant 22235002 (JC). The National Natural Science Foundation of China grant 62204138 (WS). The Outstanding Young Scientist Program of Beijing Colleges and Universities grant JWZQ20240101015 (JC). Interdisciplinary Research Project for Young Teachers of USTB (Fundamental Research Funds for the Central Universities) grant FRF-IDRY-23-006 (SD).

Conflicts of Interest

The authors declare no conflict of interest.

Data Availability Statement

The data that support the findings of this study are available in the supplementary material of this article.

References

1. J. Y. Park, D. H. Choe, D. H. Lee, et al., "Revival of Ferroelectric Memories Based on Emerging Fluorite-Structured Ferroelectrics," *Advanced Materials* 35 (2023): 2204904, https://doi.org/10.1002/adma.202204904.

2. W. Yang, C. Yu, H. Li, et al., "Ferroelectricity of Hafnium Oxide-based Materials: Current Status and Future Prospects from Physical Mechanisms to Device Applications," *Journal of Semiconductors* 44 (2023): 053101, https://doi.org/10.1088/1674-4926/44/5/053101.

3. H. Lu, D.-J. Kim, H. Aramberri, et al., "Electrically Induced Cancellation and Inversion of Piezoelectricity in Ferroelectric Hf0.5Zr0.5O2," *Nature Communications* 15 (2024): 860, https://doi.org/10.1038/s41467-024-44690-9.

4. S.-J. Yoon, D.-H. Min, S.-E. Moon, K. S. Park, J. I. Won, and S.-M. Yoon, "Improvement in Long-Term and High-Temperature Retention Stability of Ferroelectric Field-Effect Memory Transistors with Metal–Ferroelectric–Metal–Insulator–Semiconductor Gate-Stacks Using Al-Doped HfO 2 Thin Films," *IEEE Transactions on Electron Devices* 67 (2020): 499–504, https://doi.org/10.1109/TED.2019.2961117.

5. J. Zhou, Z. Zhou, X. Wang, et al., "Temperature Dependence of Ferroelectricity in Al-Doped HfO 2 Featuring a High Pr of 23.7 μC/cm 2," *IEEE Transactions on Electron Devices* 67 (2020): 5633, https://doi.org/10.1109/TED.2020.3032350.

6. B. Ku, Y. Ma, H. Han, W. Xuan, and C. Choi, "Effects of Etching Process and Annealing Temperature on the Ferroelectric Properties of Atomic Layer Deposited Al-doped HfO 2 Thin Film," *Nanotechnology* 33 (2022): 425205, https://doi.org/10.1088/1361-6528/ac7cf7.

7. I. Fina and F. Sánchez, "Epitaxial Ferroelectric HfO 2 Films: Growth, Properties, and Devices," *ACS Applied Electronic Materials* 3 (2021): 1530–1549, https://doi.org/10.1021/acsaelm.1c00110.

8. M. Lederer, D. Lehninger, T. Ali, and T. Kämpfe, "Review on the Microstructure of Ferroelectric Hafnium Oxides," *Physica Status Solidi (RRL)—Rapid Research Letters* 16 (2022): 2200168, https://doi.org/10.1002/pssr.202200168.

9. J. F. Ihlefeld, S. T. Jaszewski, and S. S. Fields, "A Perspective on Ferroelectricity in Hafnium Oxide: Mechanisms and Considerations Regarding Its Stability and Performance," *Applied Physics Letters* 121 (2022): 240502, https://doi.org/10.1063/5.0129546.

10. X. Liu, L. Yao, Y. Cheng, B. Xiao, M. Liu, and W. Wang, "Observing Large Ferroelectric Polarization in Top-electrode-free Al:HfO2 Thin Films with Al-rich Strip Structures," *Applied Physics Letters* 115 (2019): 152901, https://doi.org/10.1063/1.5110668.

11. Y. Zheng, Y. Zhang, T. Xin, et al., "Direct Atomic-scale Visualization of the 90° Domain Walls and Their Migrations in Hf0.5Zr0.5O2 Ferroelectric Thin Films," *Materials Today Nano* 24 (2023): 100406, https://doi.org/10.1016/j.mtnano.2023.100406.

12. H. Mulaosmanovic, E. T. Breyer, T. Mikolajick, and S. Slesazeck, "Reconfigurable Frequency Multiplication with a Ferroelectric Transistor," *Nature Electronics* 3 (2020): 391–397, https://doi.org/10.1038/s41928-020-0413-0.

13. Z. Zihao, Z. Bangmin, and Z. Yue, "Progress on hafnium oxide-based emerging ferroelectric materials and applications," *Microstructures* 5 (2025): 2025095.

14. Y. Wang, L. Tao, R. Guzman, et al., "A Stable Rhombohedral Phase in Ferroelectric Hf(Zr) 1+X O 2 Capacitor with Ultralow Coercive Field," *Science* 381 (2023): 558–563, https://doi.org/10.1126/science.adf6137.

15. X. Sang, E. D. Grimley, T. Schenk, U. Schroeder, and J. M. LeBeau, "On the Structural Origins of Ferroelectricity in HfO2 Thin Films," *Applied Physics Letters* 106 (2015): 162905, https://doi.org/10.1063/1.4919135.

16. J. Tang, F. Zhang, P. Zoogman, et al., "Martensitic Phase Transformation of Isolated HfO 2 , ZrO 2 , and Hf X Zr 1−x O 2 (0< x

< 1) Nanocrystals," *Advanced Functional Materials* 15 (2005): 1595–1602, https://doi.org/10.1002/adfm.200500050.

17. L. Ma, J. Wu, T. Zhu, Y. Huang, Q. Lu, and S. Liu, "Ultrahigh Oxygen Ion Mobility in Ferroelectric Hafnia," *Physical Review Letters* 131 (2023): 256801, https://doi.org/10.1103/PhysRevLett.131.256801.

18. T. D. Huan, V. Sharma, G. A. Rossetti, and R. Ramprasad, "Pathways towards Ferroelectricity in hafnia," *Physical Review B* 90 (2014): 064111, https://doi.org/10.1103/PhysRevB.90.064111.

19. Y. Wei, P. Nukala, M. Salverda, et al., "A Rhombohedral Ferroelectric Phase in Epitaxially Strained Hf0.5Zr0.5O2 Thin Films," *Nature Materials* 17 (2018): 1095–1100, https://doi.org/10.1038/s41563-018-0196-0.

20. C.-K. Lee, E. Cho, H.-S. Lee, C. S. Hwang, and S. Han, "First-principles Study on Doping and Phase Stability of HfO2," *Physical Review B* 78 (2008): 012102, https://doi.org/10.1103/PhysRevB.78.012102.

21. Y. Qi, S. Singh, C. Lau, et al., "Stabilization of Competing Ferroelectric Phases of HfO2 under Epitaxial Strain," *Physical Review Letters* 125 (2020): 257603, https://doi.org/10.1103/PhysRevLett.125.257603.

22. U. Schroeder, M. H. Park, T. Mikolajick, and C. S. Hwang, "The Fundamentals and Applications of Ferroelectric HfO2," *Nature Reviews Materials* 7 (2022): 653–669, https://doi.org/10.1038/s41578-022-00431-2.

23. Z. Sirui, M. Xinpeng, Y. Qijun, et al., "Atomic Structure of the Phase Interface in Hafnium Oxide-Based Thin Films," *Microstructures* 5 (2025): 2025069.

24. D.-H. Choe, S. Kim, T. Moon, et al., "Unexpectedly Low Barrier of Ferroelectric Switching in HfO2 via Topological Domain Walls," *Materials Today* 50 (2021): 8–15, https://doi.org/10.1016/j.mattod.2021.07.022.

25. Z. L. Shen, L. Zhou, Y. Xiong, et al., "Epitaxial Growth and Phase Evolution of Ferroelectric La-doped HfO2 Films," *Applied Physics Letters* 120 (2022): 162904, https://doi.org/10.1063/5.0087976.

26. X. Xu, F.-T. Huang, Y. Qi, et al., "Kinetically Stabilized Ferroelectricity in Bulk Single-crystalline HfO2:Y," *Nature Materials* 20 (2021): 826–832, https://doi.org/10.1038/s41563-020-00897-x.

27. T. Shimizu, Y. Tashiro, T. Mimura, et al., "Electric-Field-Induced Ferroelectricity in 5%Y-Doped Hf 0.5 Zr 0.5 O 2: Transformation from the Paraelectric Tetragonal Phase to the Ferroelectric Orthorhombic Phase," *Physica Status Solidi (RRL)—Rapid Research Letters* 15 (2021): 2000589, https://doi.org/10.1002/pssr.202000589.

28. Y. Tashiro, T. Shimizu, T. Mimura, and H. Funakubo, "Comprehensive Study on the Kinetic Formation of the Orthorhombic Ferroelectric Phase in Epitaxial Y-Doped Ferroelectric HfO 2 Thin Films," *ACS Applied Electronic Materials* 3 (2021): 3123–3130, https://doi.org/10.1021/acsaelm.1c00342.

29. D. Chen, Y. Dong, T. Cui, et al., "Unveiling the Polarization Switching Pathway through Tetragonal Phase as a Metastable Intermediate State in Ferroelectric Hfxzr1-Xo2 Thin Film," *Nature Communications* 16 (2025): 8188.

30. M. G. Kozodaev, A. G. Chernikova, E. V. Korostylev, et al., "Mitigating Wakeup Effect and Improving Endurance of Ferroelectric HfO2-ZrO2 Thin Films by Careful La-doping," *Journal of Applied Physics* 125 (2019): 034101, https://doi.org/10.1063/1.5050700.

31. A. G. Chernikova, M. G. Kozodaev, D. V. Negrov, et al., "Improved Ferroelectric Switching Endurance of La-Doped Hf 0.5 Zr 0.5 O 2 Thin Films," *ACS Applied Materials & Interfaces* 10 (2018): 2701, https://doi.org/10.1021/acsami.7b15110.

32. U. Schroeder, C. Richter, M. H. Park, et al., "Lanthanum-Doped Hafnium Oxide: a Robust Ferroelectric Material," *Inorganic Chemistry* 57 (2018): 2752, https://doi.org/10.1021/acs.inorgchem.7b03149.

33. T. Song, H. Tan, R. Bachelet, G. Saint-Girons, I. Fina, and F. Sánchez, "Impact of La Concentration on Ferroelectricity of La-Doped HfO 2 Epitaxial Thin Films," *ACS Applied Electronic Materials* 3 (2021): 4809, https://doi.org/10.1021/acsaelm.1c00672.

34. T. Song, R. Bachelet, G. Saint-Girons, N. Dix, I. Fina, and F. Sánchez, "Thickness Effect on the Ferroelectric Properties of La-doped HfO 2 Epitaxial Films Down to 4.5 Nm," *Journal of Materials Chemistry C* 9 (2021): 12224, https://doi.org/10.1039/D1TC02512K.

35. T. Song, R. Bachelet, G. Saint-Girons, R. Solanas, I. Fina, and F. Sánchez, "Epitaxial Ferroelectric La-Doped Hf 0.5 Zr 0.5 O 2 Thin Films," *ACS Applied Electronic Materials* 2 (2020): 3221, https://doi.org/10.1021/acsaelm.0c00560.

36. P. Jiao, H. Cheng, J. Li, et al., "Flexoelectricity-stabilized Ferroelectric Phase with Enhanced Reliability in Ultrathin La:HfO2 Films," *Applied Physics Reviews* 10 (2023): 031417, https://doi.org/10.1063/5.0144958.

37. K. P. Kelley, A. N. Morozovska, E. A. Eliseev, et al., "Ferroelectricity in hafnia Controlled via Surface Electrochemical state," *Nature Materials* 22 (2023): 1144, https://doi.org/10.1038/s41563-023-01619-9.

38. M. H. Park, T. Schenk, C. M. Fancher, et al., "A Comprehensive Study on the Structural Evolution of HfO 2 Thin Films Doped with Various Dopants," *Journal of Materials Chemistry C* 5 (2017): 4677, https://doi.org/10.1039/C7TC01200D.

39. Y. Yun, P. Buragohain, M. Li, et al., "Intrinsic Ferroelectricity in Y-doped HfO2 Thin Films," *Nature Materials* 21 (2022): 903–909, https://doi.org/10.1038/s41563-022-01282-6.

40. R. He, H. Wu, S. Liu, H. Liu, and Z. Zhong, "Ferroelectric Structural Transition in Hafnium Oxide Induced by Charged Oxygen Vacancies," *Physical Review B* 104 (2021): 180102, https://doi.org/10.1103/PhysRevB.104.L180102.

41. L.-Y. Ma and S. Liu, "Structural Polymorphism Kinetics Promoted by Charged Oxygen Vacancies in HfO2," *Physical Review Letters* 130 (2023): 096801, https://doi.org/10.1103/PhysRevLett.130.096801.

42. S. S. Cheema, D. Kwon, N. Shanker, et al., "Enhanced Ferroelectricity in Ultrathin Films Grown Directly on Silicon," *Nature* 580 (2020): 478–482, https://doi.org/10.1038/s41586-020-2208-x.

43. H. Zhong, M. Li, Q. Zhang, et al., "Large-Scale Hf 0.5 Zr 0.5 O 2 Membranes with Robust Ferroelectricity," *Advanced Materials* 34 (2022): 2109889, https://doi.org/10.1002/adma.202109889.

44. T. Mikolajick, M. H. Park, L. Begon-Lours, and S. Slesazeck, "From Ferroelectric Material Optimization to Neuromorphic Devices," *Advanced Materials* 35 (2023): 2206042, https://doi.org/10.1002/adma.202206042.

45. E. D. Grimley, T. Schenk, X. Sang, et al., "Structural Changes Underlying Field-Cycling Phenomena in Ferroelectric HfO 2 Thin Films," *Advanced Electronic Materials* 2 (2016): 1600173, https://doi.org/10.1002/aelm.201600173.

46. J. Tang, J. Fabbri, R. Robinson, et al., "Solid-Solution Nanoparticles: Use of a Nonhydrolytic Sol−Gel Synthesis To Prepare HfO 2 and Hf X Zr 1-x O 2 Nanocrystals," *Chemistry of Materials* 16 (2004): 1336–1342, https://doi.org/10.1021/cm049945w.

47. T. Zhu, L. Ma, S. Deng, and S. Liu, "Progress in Computational Understanding of Ferroelectric Mechanisms in HfO2," *Npj Computational Materials* 10 (2024): 188, https://doi.org/10.1038/s41524-024-01352-0.

48. H. J. Kim, M. H. Park, Y. J. Kim, et al., "Grain Size Engineering for Ferroelectric Hf0.5Zr0.5O2 Films by an Insertion of Al2O3 Interlayer," *Applied Physics Letters* 105 (2014): 192903, https://doi.org/10.1063/1.4902072.

49. G. Kresse and J. Furthmüller, "Efficient Iterative Schemes for Ab Initio Total-energy Calculations Using a Plane-wave Basis Set," *Physical Review B* 54 (1996): 11169, https://doi.org/10.1103/PhysRevB.54.11169.

50. P. E. Blöchl *Physical Review B* 50 (1994): 17953.

51. G. Kresse and D. Joubert, "From Ultrasoft Pseudopotentials to the Projector Augmented-wave Method," *Physical Review B* 59 (1999): 1758, https://doi.org/10.1103/PhysRevB.59.1758.

52. J. P. Perdew, K. Burke, and M. Ernzerhof, "Generalized Gradient Approximation Made Simple," *Physical Review Letters* 77 (1996): 3865, https://doi.org/10.1103/PhysRevLett.77.3865.

53. A. R. G. Oganov and W. Colin, "Crystal Structure Prediction Using Ab Initio Evolutionary Techniques: Principles and Applications," *The Journal of Chemical Physics* 124 (2006): 244704, https://doi.org/10.1063/1.2210932.

54. A. O. Lyakhov, A. R. Oganov, H. T. Stokes, and Q. Zhu, "New Developments in Evolutionary Structure Prediction Algorithm USPEX," *Computer Physics Communications* 184 (2013): 1172–1182, https://doi.org/10.1016/j.cpc.2012.12.009.

55. A. R. Oganov, A. O. Lyakhov, and M. Valle, "How Evolutionary Crystal Structure Prediction Works—And Why," *Accounts of Chemical Research* 44 (2011): 227–237, https://doi.org/10.1021/ar1001318.

56. J. Wu, Y. Zhang, L. Zhang, and S. Liu, "Deep Learning of Accurate Force Field of Ferroelectric HfO2," *Physical Review B* 103 (2021): 024108, https://doi.org/10.1103/PhysRevB.103.024108.

57. J. Wu, J. Yang, L. Ma, L. Zhang, and S. Liu, "Modular Development of Deep Potential for Complex Solid Solutions," *Physical Review B* 107 (2023): 144102, https://doi.org/10.1103/PhysRevB.107.144102.

58. S. Plimpton, "Fast Parallel Algorithms for Short-Range Molecular Dynamics," *Journal of Computational Physics* 117 (1995): 1–19, https://doi.org/10.1006/jcph.1995.1039.

59. P. P. Umari, "Ab Initio Molecular Dynamics in a Finite Homogeneous Electric Field," *Physical Review Letters* 89 (2002): 157602, https://doi.org/10.1103/PhysRevLett.89.157602.

60. S. Liu, I. Grinberg, and A. M. Rappe, "Intrinsic Ferroelectric Switching from First Principles," *Nature* 534 (2016): 360–363, https://doi.org/10.1038/nature18286.

Supporting Information

Additional supporting information can be found online in the Supporting Information section.

Supporting File: adma71976-sup-0001-SuppMat.docx